A CFD-PBM coupled model under entire turbulent spectrum for simulating a bubble column with highly viscous media

Huahai Zhang, Yuelin Wang, Ali Sayyar, Tiefeng Wang*

Beijing Key Laboratory of Green Reaction Engineering and Technology

Department of Chemical Engineering, Tsinghua University, Beijing 100084, China

Correspondence author: Tiefeng Wang (E-mail: wangtf@tsinghua.edu.cn)

Abstract

To account for the effect of liquid viscosity, the bubble breakup model considering turbulent eddy collision based on the inertial subrange turbulent spectrum was extended to the entire turbulent spectrum that included the energy-containing, inertial, and energy-dissipation subranges. The computational fluid dynamics-population balance model (CFD-PBM) coupled model was modified to include this extended bubble breakup model for simulations of a bubble column. The effect of turbulent energy spectrum on the bubble breakup and hydrodynamic behaviors was studied in a bubble column under different liquid viscosities. The results showed that when the liquid viscosity was < 80 mPa·s, the bubble breakup and hydrodynamics were almost independent on the turbulent spectrum. At liquid viscosity > 80 mPa·s, the bubble breakup rate and gas holdup were significantly under-predicted when the inertial turbulent spectrum was used, and when using the entire turbulent spectrum the predictions were more consistent with experimental data.

Key words: Bubble breakup model; Inertial turbulent spectrum; Entire turbulent spectrum; CFD-PBM coupled model; Bubble column; Liquid viscosity

1. Introduction

Bubble column reactors are widely used in chemical, biochemical and petrochemical industrial processes because of their excellent characteristics, such as simple geometry, low operating and maintenance cost, and high heat and mass transfer rates.[1] Commercial reactors are often operated with highly viscous media. For example, the heavy Tellus oil (μ_l = 75 m·Pas) was synthesized from synthesis gas in gas-liquid-solid three-phase slurry reactors.[2,3] A high concentration of fine particles would greatly increase the apparent viscosity of pseudo-homogeneous slurry phase in slurry reactors.[4] Experiments showed that liquid viscosity μ_l played an important role on the hydrodynamics and mass transport behaviors of bubble columns.[5-10] At high μ_l, the bubble breakup rate significantly decreased,[11] leading to a wider bubble size distribution and lower gas holdup and gas-liquid mass transfer rate.[9,10,12] Kajero et al.[8] studied the viscous effects on flow regime and bubble dynamic behaviors using silicone oil ($\mu_l \geq$ 5000 mPa·s) by electrical capacitance tomography (ECT), and found that with increasing viscosity the occurrence of spherical cap bubbles decreased, while the tendency of slug flow increased. Liu et al.[13] reported that with increasing μ_l, the bubble plume oscillation frequency in a bubble column increased at low superficial gas velocity (U_g < 0.08 m/s), but decreased when U_g > 0.08 m/s and in high liquid viscosity range.

The computational fluid dynamics (CFD) incorporating population balance model (PBM) has been demonstrated effective to quantitatively predict the hydrodynamics and mass transport behaviors of the bubble column.[14-25] In the CFD-PBM coupled

model, the CFD model gives the flow field and phase holdup and the PBM gives the local bubble size distribution. The hydrodynamics and mass transport behaviors of bubble columns with low liquid viscosity media have been successfully predicted by the CFD-PBM coupled model based on Kolmogorov inertial subrange turbulent spectrum.[9,14,26-31] However, the simulations of bubble columns with high liquid viscosity are very limited.

Wilkinson et al.[11] experimentally reported that the liquid viscosity was closely related to bubble breakup behaviors, and increased μ_l reduced the bubble breakup rate. In a fully turbulent flow, the dominant bubble breakup was due to collision by turbulent eddies.[29,32-37] The bubble breakup models in previous literature[38,39] were mainly based on Kolmogorov inertial subrange turbulent energy spectrum. In these models, the lower integration limit was estimated by the minimum size of eddies in the inertial subrange, equal to 11.4-31.4 times the Kolmogorov scale $\eta = (\mu_l/\rho_l)^{3/4}\varepsilon^{-1/4}$. With increasing μ_l, this minimum size of turbulent eddies increased and the effective inertial energy spectrum narrowed, resulting in considerably decreased bubble breakup rate. While, with continuously increasing μ_l, the inertial subrange would disappear. In this case, the breakup model only considering the energy from inertial subrange was not applicable in the industrial turbulent dispersed multiphase flows. Recently, many researchers[39-43] have rebuilt their breakup model under the entire turbulent energy spectrum including the energy-dissipation, inertial and energy-containing ranges. They found that the turbulent eddies in the energy-dissipation and energy-containing zones could also induce bubble breakup. With the CFD-PBM model based on the entire turbulent

spectrum, Castellano et al.[44] and Niño et al.[45] simulated a liquid-liquid and a gas-liquid stirred tank reactor, respectively, and they both found that the effect of energy spectrum was significant. After considering the entire turbulent spectrum, the predicted bubble or drop Sauter diameters and mass transfer coefficients $k_l a$ were more consistent with experimental data.[44,45] However, the simulations of gas-liquid bubble columns with a CFD-PBM model under entire turbulent spectrum have not been studied, and the researches on the applicability of inertial or entire energy spectrum under different liquid viscosity ranges are also limited.

The present work aimed to extend our previous bubble breakup model[29] to the entire turbulent energy spectrum, and incorporate this extended bubble breakup model in the CFD-PBM coupled model to simulate a bubble column under a wide liquid viscosity range. The applicability of the CFD-PBM coupled model based on entire turbulent spectrum was studied, and the critical liquid viscosity where the entire turbulent spectrum must be used to replace the inertial turbulent spectrum was obtained.

2. Bubble breakup model development

2.1 Entire turbulent energy spectrum model and number density of eddies

To extend our bubble breakup model[29] from inertial turbulent spectrum to entire turbulent spectrum, the mean turbulent eddy velocity $\bar{u}_\lambda$ and the number density of eddies n_λ with eddy size of λ under entire turbulent spectrum range should be calculated in advance. They were both the necessary terms to derive the model of bubble breakup in a turbulent flow.[32,33,40,42]

The turbulent kinetic energy of spherical eddies with size from λ to $\lambda + d\lambda$ per unit mass of liquid was equal to the kinetic energy of eddies of wave number from κ to $\kappa + d\kappa$, with $\kappa = 2\pi/\lambda$,[32,46,47] as follows:

$$n_\lambda \cdot \rho_l \frac{\pi}{6}\lambda^3 \cdot \frac{1}{2}\overline{u}_\lambda^2 d\lambda = E(\kappa)\rho_l(-d\kappa) \tag{1}$$

where $\overline{u}_\lambda$ was the mean turbulent velocity, and $E(\kappa)$ was the turbulent energy spectrum.

The model of entire spectrum that includes the energy-dissipating, inertial and energy-containing subranges of isotropic turbulence proposed by Pope[47] was used:

$$E(\kappa) = C_1\varepsilon^{2/3}\kappa^{-5/3} f_L(\kappa L)\, f_\eta(\kappa\eta) \tag{2}$$

$$f_L(\kappa L) = \left\{ \frac{\kappa L}{\left[(\kappa L)^2 + C_L\right]^{1/2}} \right\}^{5/3+p_0} \tag{3}$$

$$f_\eta(\kappa\eta) = \exp\left\{ -\beta\left(\left[(\kappa\eta)^4 + C_\eta^4 \right]^{1/4} - C_\eta \right) \right\} \tag{4}$$

where $f_L(\kappa L)$ and $f_\eta(\kappa\eta)$ are specified dimensionless functions that determine the shapes of the energy-containing and energy-dissipating subranges, respectively. C_1 = 1.5, P_0 = 2 and β = 5.2 are model constant parameters.[47] L is the integral scale, and η is the Kolmogorov scale[46]:

$$L = k^{3/2}/\varepsilon \tag{5}$$

$$\eta = \left(\nu^3/\varepsilon\right)^{1/4},\ \nu = \mu_l/\rho_l \tag{6}$$

$$k = \int_0^\infty E(\kappa)d\kappa \tag{7}$$

$$\varepsilon = \int_0^\infty 2\nu\kappa^2 E(\kappa)d\kappa \tag{8}$$

The positive parameters C_L and C_η are determined by computing the integrals of Eqs. (7) and (8), respectively, as suggested by Solsvik et al.[48]:

$$C_\eta(\mathrm{Re}_\lambda, C_0) = \exp\left[\frac{14.043 - 4.222C_0}{\mathrm{Re}_\lambda^{1.986-0.363C_0}} \right] - 0.089 - 0.339C_0 \tag{9}$$

$$C_L(\mathrm{Re}_\lambda, C_0) = \exp\left[-\frac{4.478 + 18.362C_0}{\mathrm{Re}_\lambda^{1.075-0.070C_0}} - 1.342 + 2.024C_0 \right] - 1.913 + 2.169C_0 \quad (10)$$

where Reλ was the Taylor-scale Reynolds number, $\mathrm{Re}_\lambda = \sqrt{20/3}\left(k^{1/2}L/\nu\right)^{1/2}$, and C_0 was a parameter having a value of 1.40~1.75.

Generally, $\overline{u}_\lambda^2$ could be approximated by the application of the second-order longitudinal structure function $\langle[\delta v]^2\rangle(\lambda)$.[39] The function $\langle[\delta v]^2\rangle(\lambda)$ proposed by Davidson et al.[49] was used:

$$\langle[\delta v]^2\rangle(\lambda) = \frac{4}{3}\int_{-\infty}^{\infty} E(\kappa)\left[1 - 3\left\{\frac{\sin(\kappa\lambda)}{(\kappa\lambda)^3} - \frac{\cos(\kappa\lambda)}{(\kappa\lambda)^2}\right\}\right] d\kappa \quad (11)$$

Following Solsvik and Jakobsen[50], the analytical solution for Eq. (11) was calculated as follows:

$$\langle[\delta v]^2\rangle(\lambda) = \tfrac{4}{3}k\left\{1 - \left[T_1(\lambda) + T_2(T_3(\lambda)T_4(\lambda) - T_5(\lambda))\right]\right\} \quad (12)$$

$$T_1(\lambda) = \frac{2}{[S(\lambda)]^2} F\left(\left(-\tfrac{1}{3}\right)^{1/2}, \left(\tfrac{3}{2}\right) \middle| \frac{[S(\lambda)]^2}{4}\right) \quad (13)$$

$$T_2 = 5.2\Gamma\left(\tfrac{2}{3}\right) \quad (14)$$

$$T_3(\lambda) = 27 \times 2^{1/3}[S(\lambda)]^{2/3}\Gamma\left(\tfrac{2}{3}\right) \quad (15)$$

$$T_4(\lambda) = \frac{1}{325\pi} F\left(\left(\tfrac{7}{3}\right)^{11/6}, \left(\tfrac{17}{6}\right) \middle| \frac{[S(\lambda)]^2}{4}\right) \quad (16)$$

$$T_5(\lambda) = \frac{2^{2/3}}{2\pi[S(\lambda)]^{2/3}} K_{\frac{4}{3}}\left(S(\lambda)\right) \quad (17)$$

$$S(\lambda) = \frac{\kappa\lambda}{c_L^{-1/2}\kappa L} \quad (18)$$

where F, K and Γ are hypergeometric, Bessel and gamma functions, respectively. The final solution covering the entire spectrum[39] was obtained by adding the energy-dissipation subrange spectrum (Sawford and Hunt[51]):

$$\langle[\delta v]^2\rangle(\lambda) = \tfrac{4}{3}k\left[\frac{\lambda^2}{\lambda_d^2 + \lambda^2}\right]^{2/3}\left\{1 - \left[T_1(\lambda) + T_2(T_3(\lambda)T_4(\lambda) - T_5(\lambda))\right]\right\} \quad (19)$$

where $\lambda_d = (15C)^{3/4}\eta$, and $C = 2$.

Therefore, the mean turbulent velocity $\bar{u}_\lambda$ was obtained:

$$\bar{u}_\lambda = \sqrt{\frac{4}{3}k\left[\frac{\lambda^2}{\lambda_d^2+\lambda^2}\right]^{2/3}\left\{1-\left[T_1(\lambda)+T_2\left(T_3(\lambda)T_4(\lambda)-T_5(\lambda)\right)\right]\right\}} \tag{20}$$

By substituting Eqs. (20) and (2) into Eq. (1), the number density of eddies under the entire turbulent spectrum was expressed as[39]:

$$n_\lambda = \frac{24C_1\varepsilon^{2/3}\lambda^{-10/3}f_L(\frac{2\pi}{\lambda}L)f_\eta(\frac{2\pi}{\lambda}\eta)}{(2\pi)^{5/3}\left\{\frac{4}{3}k\left[\frac{\lambda^2}{\lambda_d^2+\lambda^2}\right]^{2/3}\left\{1-\left[T_1(\lambda)+T_2\left(T_3(\lambda)T_4(\lambda)-T_5(\lambda)\right)\right]\right\}\right\}} \tag{21}$$

2.2 Extended bubble breakup model

Analogous to the models from Luo and Svendsen[32], Wang et al.[34] and Andersson and Andersson[52], our previous bubble breakup model[29] was constructed by multiplying a collision or interaction frequency term by a probability density function based on inertial subrange turbulent spectrum of turbulence. The main equations of our previous bubble breakup model are listed in Table 1. After replacing the number density and mean turbulent velocity of eddies under inertial turbulent spectrum with that under entire turbulent spectrum, the bubble breakup model was extended to the entire turbulent spectrum, as listed in Table 1.

Table 2. Liquid properties in this work.

Liquids	ρ_l, kg/m^3	μ_l, mPa·s	σ_l, mN/m
Water	1000	1.0	72.5
54.9 wt% glycerol solution	1124	7.9	63.6
69.9 wt% glycerol solution	1140	20.1	63.2
76.6 wt% glycerol solution	1184	39.6	62.0
Glucose solution A	1340	170.0	76.0
Glucose solution B	1380	550.0	76.0

Table 1. Summary of original bubble breakup model and modified equations for model extension.

Items		Formulations	Extensions
Breakup rate without internal flow through the bubble neck	Specific rate that a bubble of size d_b breaks up with a breakup fraction of f'_v	$\Omega(f'_v\|d_b)=\int_{\lambda_{min}}^{\lambda_{max}} P_b(f'_v\|d_b,\lambda)\varpi_\lambda(d_b)d\lambda$	
	Probability density function $P_b(f'_v\|d_b, \lambda)$	$P_b(f'_v\|d_b,\lambda)=1-\int_0^{\chi_c}\exp(-\chi)d\chi=\exp(-\chi_c)$	
	Critical dimensionless energy for the breakup	$\chi_c=\frac{\max(c_f,c_d)\pi d_b^2\sigma}{1/2\rho_l\bar{u}_\lambda^2\pi\lambda^3/6}\begin{cases}1, & \lambda\le d_b\\ 1/\left(4(\lambda/d_b)^2\sin^4(\pi d_b/(4\lambda))\right), & \lambda>d_b\end{cases}$, $\bar{u}_\lambda=\sqrt{2}(\varepsilon\lambda)^{1/3}$	$\bar{u}_\lambda$ = Eq.(20)
	Energy constraint and capillary force constraint	$c_f=(f'_v)^{2/3}+(1-f'_v)^{2/3}-1$, $c_d=(\min(f'_v,1-f'_v))^{-1/3}-1$	
	Collision frequency $\varpi_\lambda(d_b)$	$\varpi_\lambda(d_b)=\frac{\pi}{4}(d_b+\lambda)^2\bar{u}_\lambda n_\lambda n,\ (\lambda\le d_b)$, $n_\lambda=0.822(1-\alpha_g)\lambda^{-4}$,	$\bar{u}_\lambda$ = Eq.(20) n_λ = Eq.(21)
		$\varpi_\lambda(d_b)=\frac{\pi d_b^3/6}{\max(\tau_e,\lambda/\bar{u})}n_\lambda n,(\lambda>d_b)$, $\bar{u}=2\lambda/d_b\sin^2(\pi/(4\lambda/d_b))\bar{u}_\lambda$, $\tau_e=\lambda^{2/3}/\varepsilon^{1/3}$	$\bar{u}_\lambda$ = Eq.(20) n_λ = Eq.(21)
Model of internal flow through bubble neck	Time for the smaller part to completely flow into the larger part, t_1, and time t_2 for the bubble neck to shrink to d_c	$t_1=\frac{V_1}{U_{neck}\pi d_{neck}^2/4}$, $t_2=\begin{cases}\frac{d_{neck}-d_{c0}}{U_{plus}+\bar{u}_\lambda}, & U_{plus}+\bar{u}_\lambda>0\\ +\infty, & U_{plus}+\bar{u}_\lambda\le 0\end{cases}$, $\bar{u}_\lambda=\sqrt{2}(\varepsilon\lambda)^{1/3}$	$\bar{u}_\lambda$ = Eq.(20)
Bubble breakup rates and daughter bubble size distribution	Breakup probability function considering the internal flow	$\gamma=\exp(-t_2/t_1)$, $f_{v,min}=\gamma f'_v$, $f_{v,max}=0.5$	
	Probability of a bubble with size d_b breaking with breakup fraction f_v under the effect of internal flow	$P_b(f_v\|d_b,f'_v)=\begin{cases}\frac{5\exp(-5fv)}{\exp(-5f_{v,min})-\exp(-5f_{v,max})}, & f_{v,min}\le f_v\le f_{v,max}\\ 0, & \text{else}\end{cases}$	
	Specific breakup rate of a bubble with size d breaking with a breakup fraction f_v	$\Omega(f_v\|d_b)=\int_0^{0.5}\Omega(f'_v\|d_b)P_b(f_v\|d_b,f'_v)\gamma df'_v,(f_v\ge f_{v,min})$	
	Total bubble breakup rate $\Omega(d_b)$, specific breakup rate $b(d_b)$, and daughter size distribution $\beta(f_v,d_b)$	$\Omega(d_b)=\int_0^{0.5}\Omega(f_v\|d_b)df_v$, $b(d_b)=\Omega(d_b)/n$, $\beta(f_v,d_b)=\Omega(f_v\|d_b)/\int_0^{0.5}\Omega(f_v\|d_b)df_v$	

3. Experimental data and methods

3.1 Experimental data

To validate the predicted effect of turbulent energy spectrum on the hydrodynamics of air-water bubble column under different pressures, the gas holdup data from Wilkinson and Dierendonck[53], Degaleesan et al.[54], Rudkevitch and Macchi[55] and Esmaeili et al.[6] were used. Furthermore, the gas holdup data from Xing et al.[9] and Urseanu et al.[5] were used to validate the effect of energy spectrum on the hydrodynamics of a bubble column at different liquid viscosity. The physical properties of used liquids are listed in Table 2.

3.2 Methods

The CFD-PBM coupled model became more complicated and the computational time and cost increased significantly after the bubble breakup model was extended to the entire turbulent spectrum. Therefore, there exists a question when it is necessary to consider the entire turbulent spectrum for predicting the bubble breakup and simulating the hydrodynamics of a bubble column rather than limiting the model to the inertial turbulent subrange. Karimi and Andersson[40] proposed a two-step verification method to clarify this question. First, the turbulent properties, e.g., the number density of eddies were needed, and then the specific breakup rates were compared with the experimental data. However, the turbulence properties and experimental bubble breakup rates were especially limited. Here, we proposed a novel approach to answer this question. The gas holdups simulated by the CFD-PBM

coupled model with the bubble breakup model under inertial subrange and entire turbulent spectrum were compared with the experimental data, and then whether the inertial subrange should be extended to the entire range was determined. The criteria obtained could be used to determine whether the entire turbulent spectrum must be considered. Because the experimental data of gas holdup of bubble columns were extensive and reliable in the literature, this approach was more feasible and effective.

4. Modeling and simulations

4.1. CFD-PBM coupled model

Figure 1 shows the coupling algorithm between the CFD two-fluid model and the PBM, which was similar to our previous work[26,28-30], except that the entire and inertial bubble breakup models in Section 2.2 were used for detailed comparison.

The governing equations of the time-averaged two-fluid model are listed in Table 3. These equations were solved using Fluent 14.0 by setting the volume fraction of bubble group i in the gas holdup, f_i, as a User Defined Scalar. The coupling of PBM was based on the following equation:

$$\begin{aligned}\nabla\cdot\left(\alpha_{\mathrm{g}}\mathbf{u}_{\mathrm{b}}f_i\right)=&\sum_{\substack{j,\mathrm{k}\\ x_{i-1}\le\left(x_j+x_{\mathrm{k}}\right)\le x_{i+1}}}^{j\ge k}\left(1-1/2\,\delta_{j,\mathrm{k}}\right)\eta_{i,j\mathrm{k}}c_{j,\mathrm{k}}\alpha_{\mathrm{g}}f_j\alpha_{\mathrm{g}}f_{\mathrm{k}}v_i/\left(v_jv_{\mathrm{k}}\right)\\&-\alpha_{\mathrm{g}}f_i\sum_{k=1}^{M}c_{i,j}\alpha_{\mathrm{g}}f_{\mathrm{k}}/v_{\mathrm{k}}+\sum_{k=i}^{M}n_{i,\mathrm{k}}b_{\mathrm{k}}\alpha_{\mathrm{g}}f_{\mathrm{k}}v_i/v_{\mathrm{k}}-b_i\alpha_{\mathrm{g}}f_i\end{aligned}\tag{22}$$

To calculate the bubble coalescence rate $c(v,v')$, three mechanisms were included, namely collision by turbulent eddies, entrainment by bubble wake and diffierence in bubble rising velocities. For bubble breakup rate $b(v)$, the breakups due to eddy collisions in Section 2.2 and due to instability of large bubbles were included. The

equations for bubble coalescence and for bubble breakup due to instablity of large bubbles are summarized in Table 4.

Table 3. Governing equations of the two-fluid model.

Models		**Equations**
Mass conservation		$\nabla\cdot(\rho\alpha\mathbf{u})_i=0$, $i=g,l$
Momentum conservation		$\nabla\cdot(\rho\alpha\mathbf{uu})_i=-\alpha_i\nabla P'+\nabla\cdot\left(\alpha\mu_{\text{eff}}(\nabla\mathbf{u}+\nabla\mathbf{u}^T)\right)_i+\mathbf{F}i,j+(\rho\alpha)_i\mathbf{g}$, $i=g,l$
k-ε turbulence mode for liquid phase	k equation	$\nabla\cdot(\rho_l\alpha_l k_l\mathbf{u}_l)_i=\nabla\cdot\left(\alpha_l\left(\mu_{\text{lam},l}+(\mu_{\text{t},l}+\mu_{\text{tb}})/\sigma_k\right)\nabla k_l\right)+\alpha_l(G_{k,l}-\rho_l\varepsilon_l)$
	ε equation	$\nabla\cdot(\rho_l\alpha_l\varepsilon_l\mathbf{u}_l)_i=\nabla\cdot\left(\alpha_l\left(\mu_{\text{lam},l}+(\mu_{\text{t},l}+\mu_{\text{tb}})/\sigma_\varepsilon\right)\nabla\varepsilon_l\right)+\alpha_l\frac{\varepsilon_l}{k_l}(C_{\text{s}1}G_{k,l}-C_{\text{s}2}\rho_l\varepsilon_l)$
	Generation rate and eddy viscosity	$G_{k,l}=\mu_{\text{eff},l}\nabla\mathbf{u}_l\cdot\left(\nabla\mathbf{u}_l+(\nabla\mathbf{u}_l)^{\text{T}}\right)-\frac{2}{3}\nabla\cdot\mathbf{u}_l\left(\mu_{\text{eff},l}\nabla\cdot\mathbf{u}_l+\rho_l k_l\right)$
		$\mu_{\text{t},l}=C_\mu(\rho_l k_l^2/\varepsilon_l)$
	Turbulence modification	$\mu_{\text{eff},l}=\mu_{\text{lam},l}+\mu_{\text{t},l}+\mu_{\text{tb}}$, $\mu_{\text{tb}}=C_{\mu\text{b}}\rho_l\alpha_g d_{\text{bs}}\lvert u_g-u_l\rvert$
		$k_{l,\text{t}}=k_l+k_{l,g}$, $\varepsilon_{l,\text{t}}=\varepsilon_l+\varepsilon_{l,g}$, $k_{l,g}=\frac{1}{2}\alpha_g C_{\text{VM}}u_{\text{slip}}^2$, $\varepsilon_{l,g}=\alpha_g g u_{\text{slip}}$
Turbulence viscosity of the gas Phase		$\mu_{\text{t},g}=\mu_{\text{t},l}\rho_g/\rho_l$
Interphase forces	Drag force	$F_{\text{D}}=\frac{C_{\text{D}}}{C_{\text{D}0}}\sum_{i=1}^{M}f_i\alpha_g\rho_l\frac{3C_{\text{D}i}}{4d_{bi}}(\mathbf{u}_g-\mathbf{u}_l)\lvert\mathbf{u}_g-\mathbf{u}_l\rvert$
		$C_{\text{D}i}=\max\left[24\text{Re}_i^{-1}\left(1+0.15\text{Re}_i^{0.687}\right),\frac{8}{3}Eo/(Eo+4)\right]$
		$C_{\text{D}}/C_{\text{D}0}=k_{\text{b,large}}\times k_{\text{b,small}}$, $k_{\text{b,large}}=1/\max(1.0,90.0\alpha_g f_{\text{b,large}})$,
		$k_{\text{b,small}}=\left(1-\alpha_{g,\text{small}}\right)\left[1+22\alpha_{g,\text{small}}/\left(Eo+0.4\right)\right]$
	Virtue mass force	$F_{\text{VM}}=\alpha_g\rho_l C_{\text{VM}}\frac{D}{Dt}(u_g-u_l)$, $C_{\text{VM}}=0.25$
		$F_{\text{L}}=-\sum_{i=1}^{M}f_i C_{\text{L}i}\alpha_g\rho_l(u_g-u_l)\frac{\partial u_l}{\partial r}$
	Transverse lift force	$C_{\text{L}i}=\begin{cases}\min(0.288\tanh(0121\text{Re}_i),f(Eo_i^{'})) & Eo_i^{'}<3.4\\ f(Eo_i^{'}) & 3.4<Eo_i^{'}<5.3\\ -0.29 & Eo_i^{'}>5.3\end{cases}$
		$f(Eo_i^{'})=0.00925Eo_i^{'3}-0.0995Eo_i^{'2}+1.088$
	Turbulent dispersion force	$F_{\text{TD}}=-C_{\text{TD}}\alpha_g\rho_l k_l\frac{\partial\alpha}{\partial r}$
	Wall lubrication force	$F_{\text{W}}=-\sum_{i=1}^{M}\frac{1}{2}f_i C_{\text{W}i}\alpha_g d_{\text{b}i}\left[(R-r)^{-2}-(R+r)^{-2}\right]\rho_l\left(u_g-u_l\right)^2$

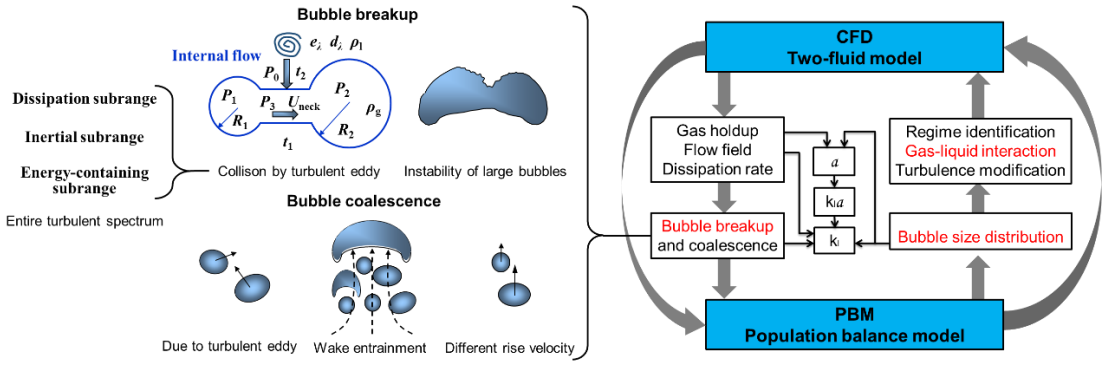

Figure 1. Schematic of the CFD-PBM coupled model

Table 4. Models of bubble breakup and coalescence.

Items		Equations
Bubble breakup due to instability of large bubbles	Breakup rate	$b(d_b)=\Omega(d_b)/n,\ \Omega(d_b)=\int_0^{0.5}\Omega(f_v\|d_b)\mathrm{d}f_v$
	Daughter bubble size distribution	$\beta(f_v,d_b)=\Omega(f_v\|d_b)/\int_0^{0.5}\Omega(f_v\|d_b)\mathrm{d}f_v$
Coalescence rate due to turbulent eddies: $c_t=\varpi_t P_t$	Collision rate	$\varpi_t(d_i,d_j)=\frac{1}{4}\pi\alpha_{g,\max}\left(\alpha_{g,\max}-\alpha_g\right)^{-1}\Gamma_{ij}\sqrt{2}\varepsilon^{1/3}\left(d_i+d_j\right)^2\left(d_i^{2/3}+d_j^{2/3}\right)^{1/2}$ $\Gamma_{ij}=l_{bt,ij}^m/(l_{bt,ij}^m+h_{bt,ij}^m),\ l_{bt,ij}=\sqrt{l_{bt,i}^2+l_{bt,j}^2},\ l_{bt}=0.89d_b,\ h_{b,ij}=(N_i+N_j)^{1/3}$
	Coalescence efficiency	$P_t(d_i,d_j)=\exp\left(-\left(0.75(1+\xi_{ij}^2)(1+\xi_{ij}^3)\right)^{1/2}(\rho_g/\rho_l+\gamma)^{-1}(1+\xi_{ij})^{-3}We_{ij}^{1/2}\right)$
Coalescence rate due to different rise velocity: $c_u=\varpi_u P_u$	Collision rate	$\varpi_u(d_i,d_j)=\frac{1}{4}\pi\alpha_{g,\max}\left(\alpha_{g,\max}-\alpha_g\right)^{-1}\sqrt{2}\varepsilon^{1/3}\left(d_i+d_j\right)^2\left(d_i^{2/3}+d_j^{2/3}\right)^{1/2}$
	Coalescence efficiency	$P_u(d_i,d_j)=0.5$
Coalescence rate due to bubble wake: $c_w=\varpi_w P_w$	Collision rate	$\varpi_w(d_i,d_j)=12.0\Theta d_i^2\bar{u}_{slip,i},\ \varpi_w(d_i,d_j)=15.4d_i^2\bar{u}_{slip,i},\ \bar{u}_{slip,i}=0.71\sqrt{gd_i}$ $\Theta=(d_j-d_c/2)^6/\left((d_j-d_c/2)^6+(d_c/2)^6\right)$ for $d_j\geq d_c/2;\ \Theta=0$ for $d_j<d_c/2$. with $d_c=4\sqrt{\sigma/(g\Delta\rho)}$
	Coalescence efficiency	$P_w(d_i,d_j)=\exp\left(-0.46\rho_l^{1/2}\varepsilon^{1/3}\sigma^{-1/2}\left(d_i d_j/(d_i+d_j)\right)^{5/6}\right)$

4.2. Simulation details

The simulations of a bubble column with 0.15 m diameter and 2.5 m height were performed in Fluent 14.0. Considering that the bubble column was axially symmetric, two-dimensional axisymmetric steady-state simulations were carried out in the present work. The results showed that the computational grid of 20 × 3 mm + 10 × 1.5 mm in the radial direction and 55 × 40 mm + 15 × 20 mm in the axial direction created by

Gambit was fine enough to be mesh independent. To solve the PBM, the bubble volume was divided into 30 groups by a geometric approach of $v_{i+1} = v_i r$ using a smallest volume $v_1=1.0 \times 10^{-10}$ m^3 and an increasing factor $r = 1.7$. Other simulation details are referred to our previous works.[26,28,30]

5. Results and discussion

5.1. Turbulent spectrum

Similar to the settings by Solsvik and Jakobsen[50], the following parameters and relations were set unless otherwise specified: $\varepsilon = 2.0$ m^2/s^3, $d_b = 0.01$ m, $L = 5d_b$, $k = (L\varepsilon)^{2/3}$, $v = \mu_l/\rho_l$, $\mathrm{Re}_L = k^{1/2}L/v$.

5.1.1 Second-order longitudinal structure function

Figure 2 shows the comparison of the Kolmogorov $\langle[\delta v]^2\rangle(\lambda)$ limited to the inertial subrange with the semi-empirical model considering the energy-containing, inertial and energy-dissipation subranges. Solsvik and Jakobsen[50] previously noted that for adequately high Re_L (~100000), the shape of structure function $\langle[\delta v]^2\rangle(\lambda)$ with entire spectrum model was consistent with the shape of Kolmogorov structure function. However, with decreasing Reynolds numbers, the range of inertial subrange narrowed and even disappeared in the curve of function $\langle[\delta v]^2\rangle(\lambda)$ under entire spectrum. In this work, it was found that the Reynolds numbers decreased considerably with increasing liquid viscosity, and these two curves shown in Fig. 2 deviated more from each other, indicating that in the high viscosity regime it caused significant error when only considering the inertial subrange in the bubble breakup

model.

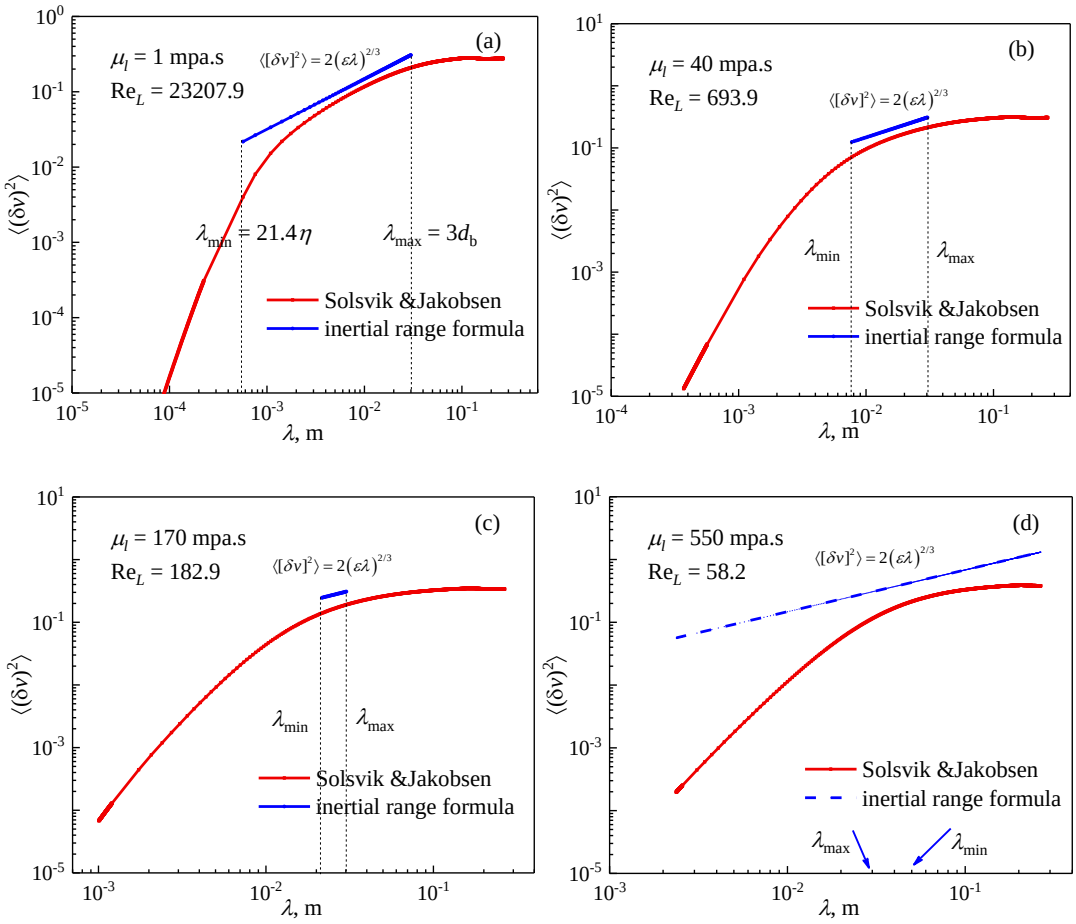

Figure 2. Effect of liquid viscosity on $\langle[\delta v]^2\rangle(\lambda)$ under inertial and entire spectrum (ε = 2.0 m^2/s^3, k = 0.2 m^2/s^2).

5.1.2 Energy spectrum

The comparison of the energy spectrum limited to the inertial subrange with that extended to the entire range is shown in Fig. 3. It can be found that the turbulent energy of eddies with middle size calculated by Kolmogorov energy spectrum was consistent with the energy calculated by the entire energy spectrum. While, with increasing liquid viscosity, the overlaps between these two spectra gradually narrowed and even disappeared.

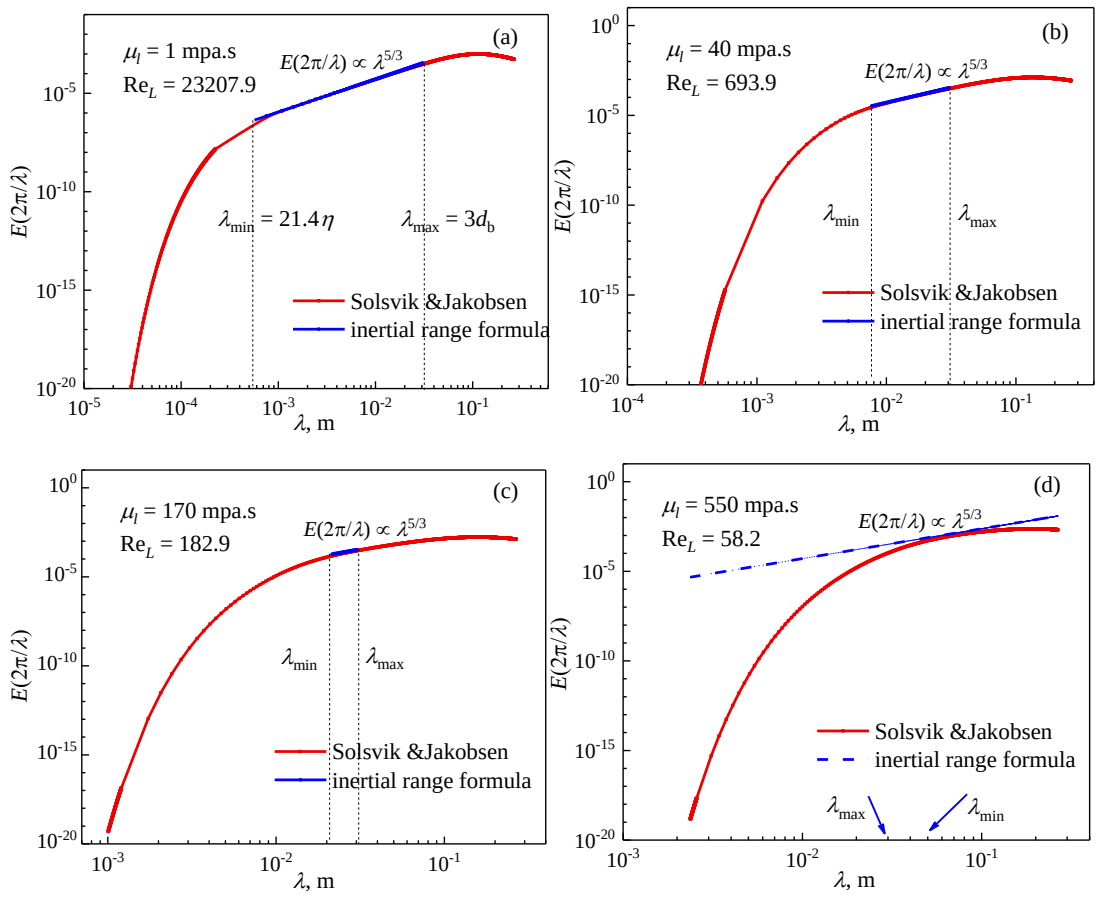

Figure 3. Effect of μ_l on the turbulent energy under inertial and entire spectrum (ε = 2.0 m^2/s^3, k = 0.2 m^2/s^2).

5.1.3. Number density of turbulent eddies

Figure 4 shows the effect of μ_l on the number density of turbulent eddies under Kolmogorov inertial spectrum and the entire spectrum. With increasing liquid viscosity, the inertial subrange narrowed, and even disappeared at liquid viscosity of 550 mPa·s. Therefore, when the inertial subrange spectrum was used, the bubble breakup rate would be zero at liquid viscosity of 550 mPa·s because λ_{min} became larger than λ_{max} in this case and no turbulent eddies satisfied the conditions in the model.

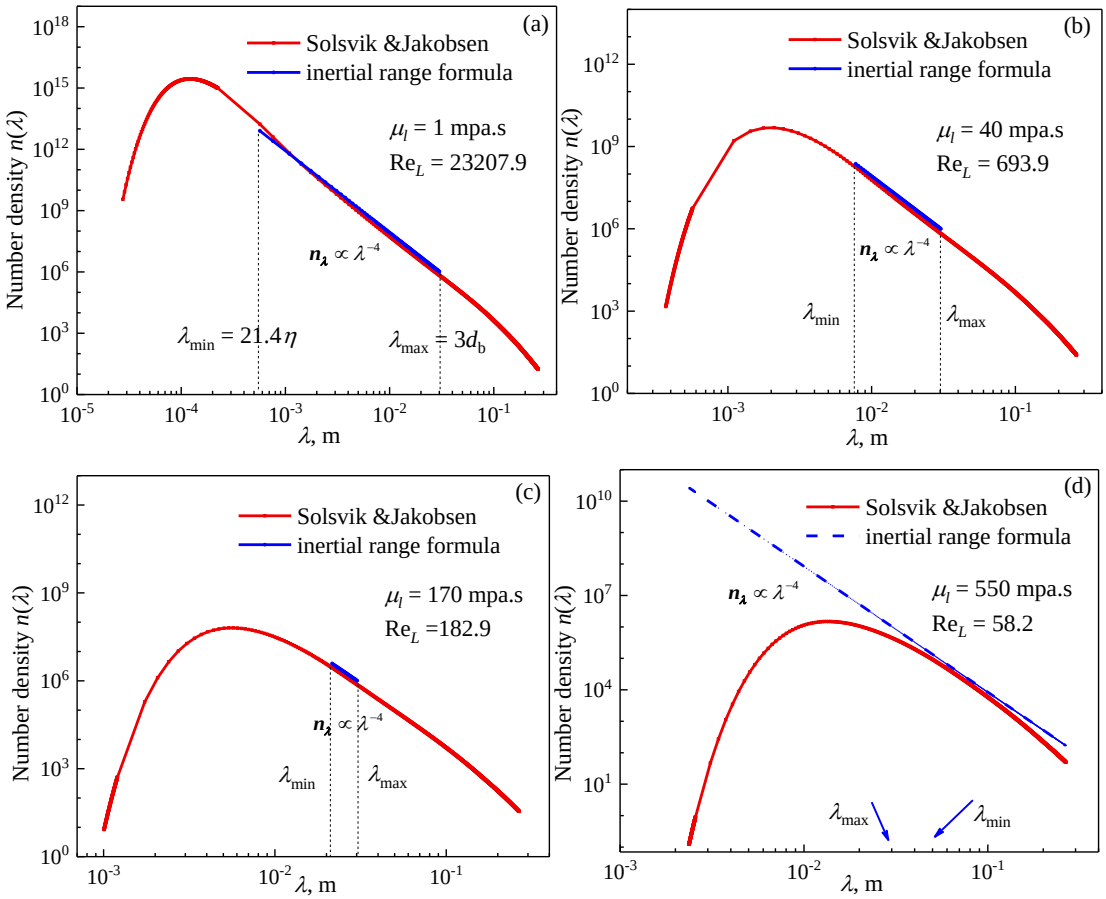

Figure 4. Effect of μ_l on the number density of turbulent eddies under inertial and entire spectrum (ε = 2.0 m^2/s^3, k = 0.2 m^2/s^2).

Figs. 3 and 4 show that there were many overlaps between the curve under entire spectrum and the line within inertial spectrum in the low viscosity regime, and Fig. 5 shows that the integral value from the energy-containing and energy-dissipation subranges was rather lower than that from the inertial subrange. However, the value of $\langle[\delta v]^2\rangle(\lambda)$ under entire turbulent spectrum was slightly lower than that under inertial spectrum, as shown in Fig. 2. In our bubble breakup model[29], the effect of pressure on the bubble breakup rate was described by considering the internal flow inside the deformed bubble. The mean turbulent velocity $\bar{u}_\lambda = \langle[\delta v]^2\rangle^{1/2}$ was important for calculations of the internal flow. There would be one question that at different

pressures whether the bubble breakup data and the hydrodynamics of bubble column under the inertial and entire spectrum were consistent in the low viscosity regime.

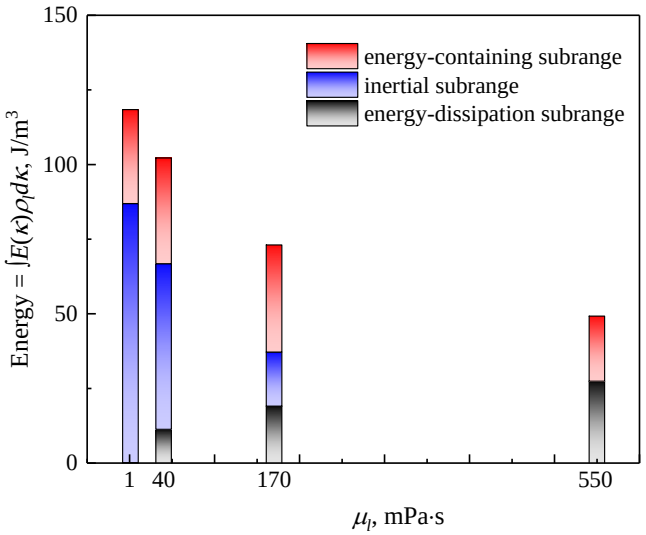

Figure 5. Effect of μ_l on the integral energy of different subranges (ε = 2.0 m^2/s^3, k = 0.2 m^2/s^2).

In the high viscosity regime, it can be seen from Figs. 2-4 that the range of inertial subrange significantly decreased with increasing liquid viscosity, and Fig. 5 shows that the energy from the energy-containing and energy-dissipation subranges became more important and larger than that from inertial subrange. Therefore, the energy-containing and energy-dissipation subranges could not be ignored in the high liquid viscosity regime. Then, another question was to determine the specific effect of the turbulent spectrum on the bubble breakup and hydrodynamics of a bubble column under different liquid viscosities.

5.2. Bubble breakup

5.2.1 Bubble breakup rate

To answer the first question in Section 5.1, the effect of gas density or pressure

on the bubble breakup rates was first investigated with the inertial and entire spectrum for the air-water system, as shown in Fig. 6. At low gas density (≤ 1 kg/m^3), the bubble breakup rates under entire spectrum were slightly lower than that under inertial spectrum. The underlying reason could be attributed to the internal flow mechanism.[29,35] During the period of internal flow, the turbulent eddies with lower velocity could not cut off the neck of bubble and cause breakup before the gas from smaller part flowed to larger part driven by Laplace pressure difference. As shown in Fig. 2, the velocity of turbulent eddies within the entire spectrum model was lower than that with the inertial spectrum model. However, at high gas density (> 1 kg/m^3), the higher breakup rates of larger mother bubbles were obtained within the entire spectrum. The critical size of mother bubbles, at which the bubble breakup rates under entire spectrum began to be larger than that under inertial spectrum, decreased with increasing gas density. With increasing gas density, the velocity of internal flow inside a deformed bubble decreased significantly especially inside large bubbles, which would weaken the effect of the different turbulent eddy velocity. Thus, the added energy from the energy-containing and energy-dissipation subranges contributed to the higher breakup rates of large bubbles under the entire spectrum. Overall, the bubble breakup rates calculated with these two turbulent spectrums were nearly consistent, which indicated that whether extending the bubble breakup model to the entire spectrum had no significant effect on the influence of gas density or pressure on the bubble breakup rates in an air-water system.

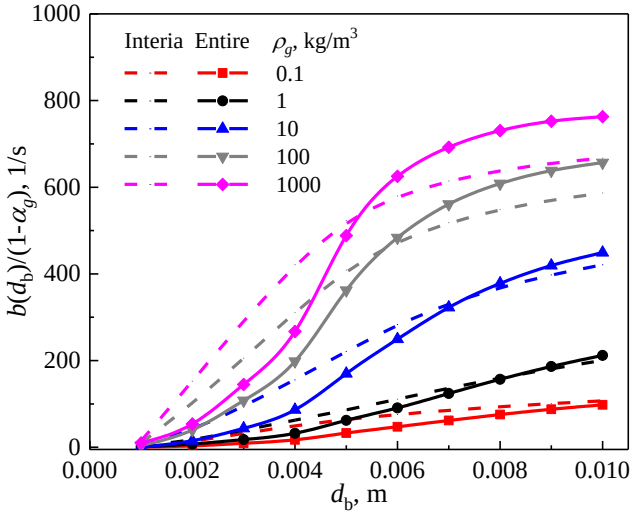

Figure 6. Effect of gas density on the bubble breakup rates under inertial and entire spectrum (ε = 2.0 m^2/s^3, μ_l = 1.0 mPa·s, σ = 72.5 mN/m).

Figure 7 shows the effects of the turbulent spectrum on the bubble breakup rates at different μ_l. It can be found that when μ_l increased to 80 mPa·s, the bubble breakup rate with the inertial subrange spectrum was significantly lower than that with the entire spectrum. In particular, the bubble breakup rates with inertial subrange spectrum approached zero at μ_l = 170 and 550 mPa·s. Therefore, the entire spectrum must be used to include the turbulent eddies in the energy-containing and dissipation subranges for the calculations of bubble breakup. The critical liquid viscosity where the bubble breakup model should be extended to entire spectrum was preliminarily determined to be ~80 mPa·s, which would be further validated by the CFD-PBM simulations in Section 5.3.

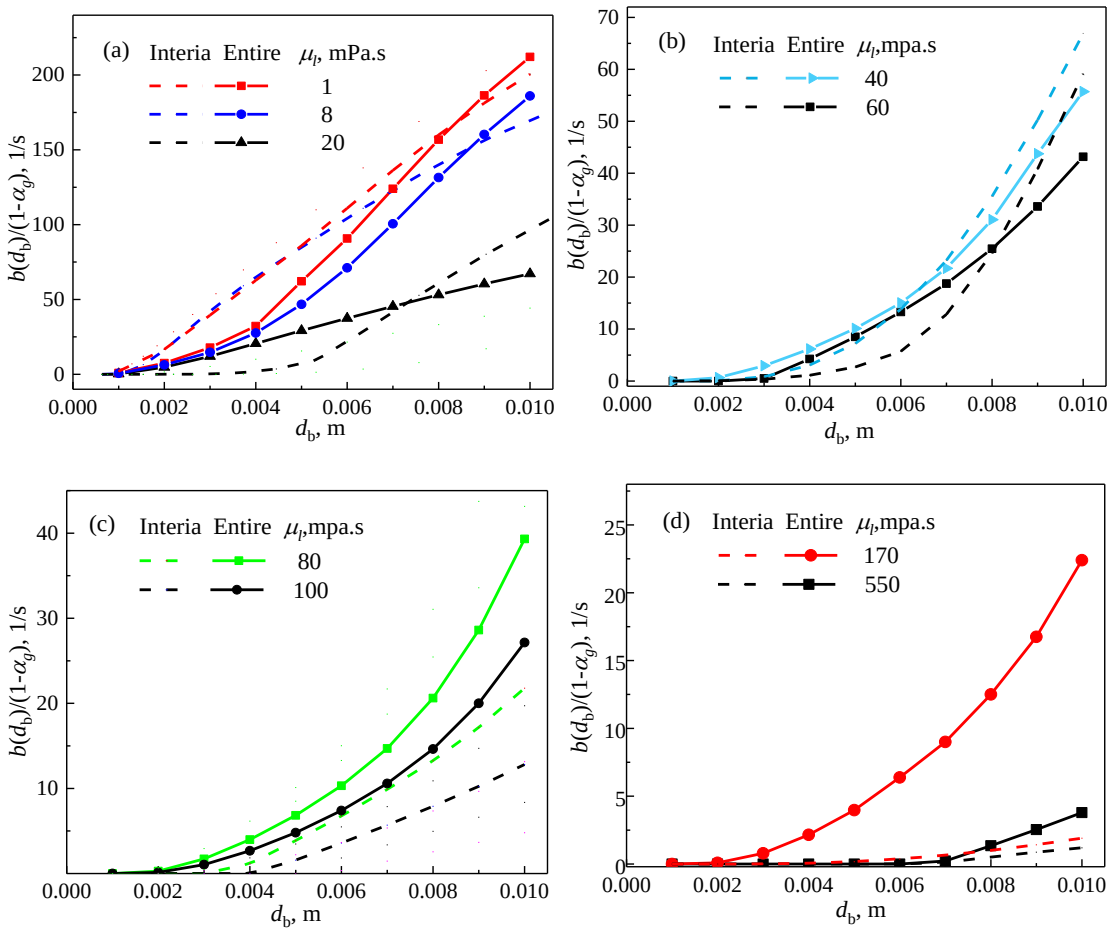

Figure 7. Effect of μ_l on bubble breakup rates under inertial and entire spectrum (ε = 2.0 m^2/s^3, ρ_g = 1 kg/m^3).

5.2.2 Daughter bubble size distribution

The influence of turbulent spectrum on the daughter bubble size distributions under different gas densities was shown in Fig. 8. The probabilities of equal-size breakup under the entire spectrum were slightly lower than that under the inertial spectrum, because the turbulent velocity of eddies within entire spectrum was lower than that within inertial spectrum, as shown in Fig. 2.

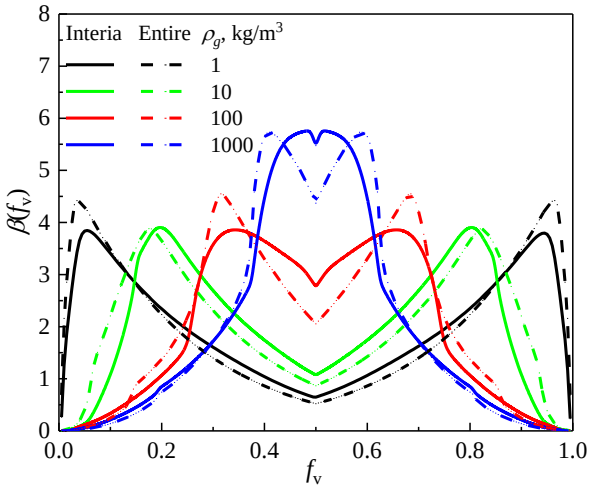

Figure 8. Effect of gas density on daughter size distribution (d_b = 6 mm, μ_l = 1.0 mPa·s, σ = 0.072 N/m, ε = 2.0 m^2/s^3).

5.3. CFD-PBM simulations

CFD-PBM simulations were carried out to further study the effect of turbulent spectrums. First, at low liquid viscosity, the effect of pressure or gas density on the average gas holdup under inertial and entire spectrum was studied, and the results are shown in Fig. 9. The increasing trend of average gas holdup with increasing pressure could be predicted by the CFD-PBM model with the entire or inertial spectrum. Although the gas holdups predicted with the entire spectrum were slightly lower than that with the inertial spectrum due to the lower bubble breakup rate, they both agreed well with the experimental data. Therefore, it was demonstrated again that the extension to the entire spectrum had no significant effect on the simulations of an air-water bubble column.

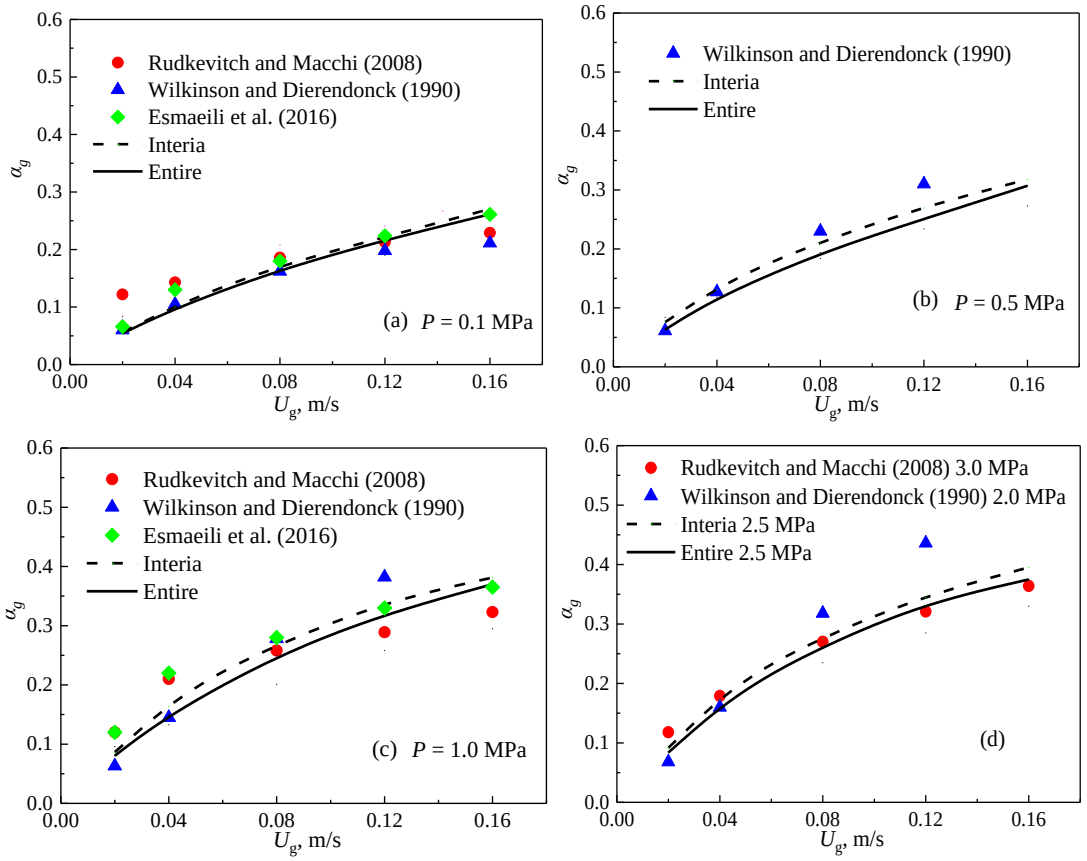

Figure 9. Comparison of the calculated average gas holdup under inertial and entire spectrum with experimental data at different pressure in an air-water system.

Figure 10 shows the effect of μ_l on the average α_g with the inertial and entire spectrum. In the low liquid viscosity regime (< 40 mPa·s), the gas holdups predicted by the CFD-PBM coupled model with either the entire or inertial spectrum were both in agreement with the experimental data. Although there were no experimental data at liquid viscosity of 60 mPa·s, the simulated gas holdups under the inertial spectrum agreed with that under entire spectrum. However, in the high liquid viscosity regime ($\geqslant$ 80 mPa·s), the predicted average gas holdups under the inertial spectrum were much lower than that under the entire spectrum. Furthermore, at liquid viscosity of 170 and 550 mPa·s, the average gas holdups predicted by the CFD-PBM coupled

model with the entire turbulent spectrum were more consistent with the experimental data reported by Urseanu et al.[5] Therefore, from the view of the simulations of a bubble column, it was necessary to extend bubble breakup model to the entire turbulent spectrum in the high liquid viscosity regime, and the critical liquid viscosity of ~80 mPa·s was further confirmed.

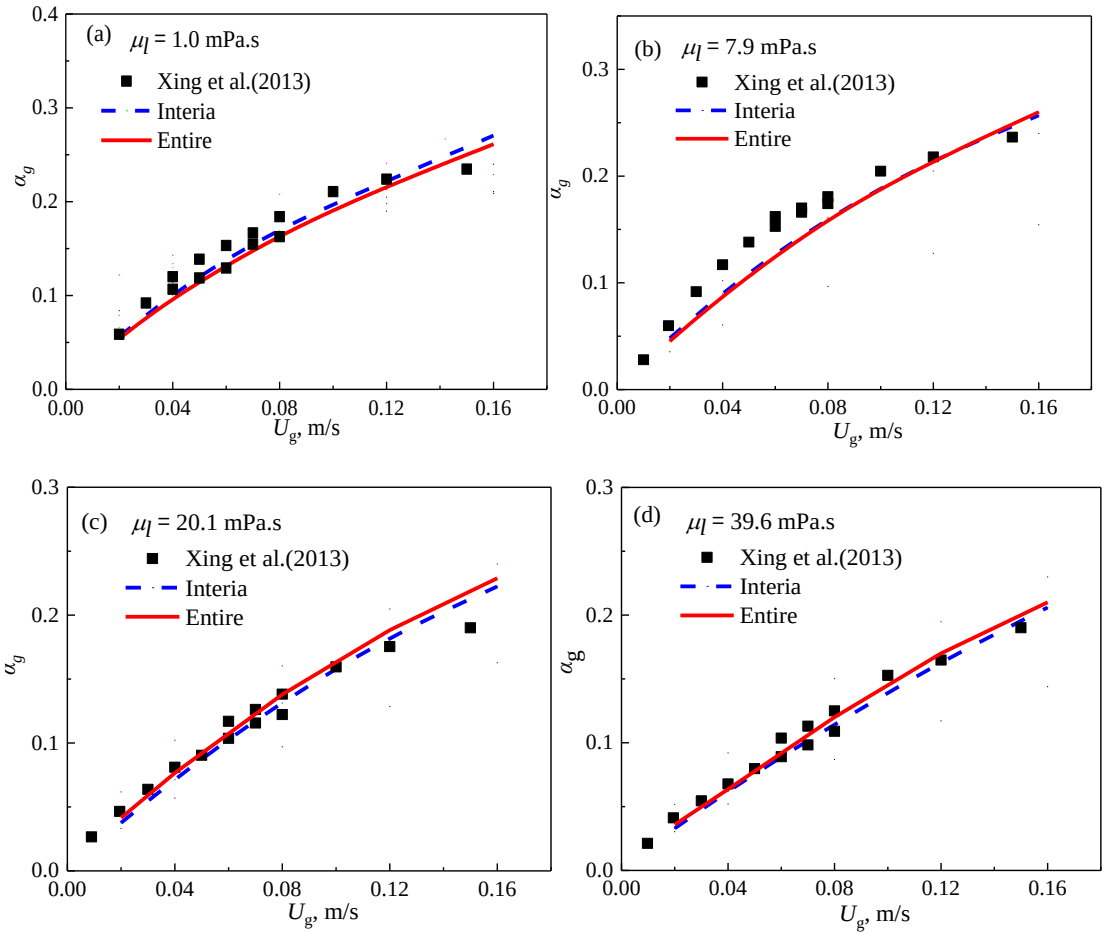

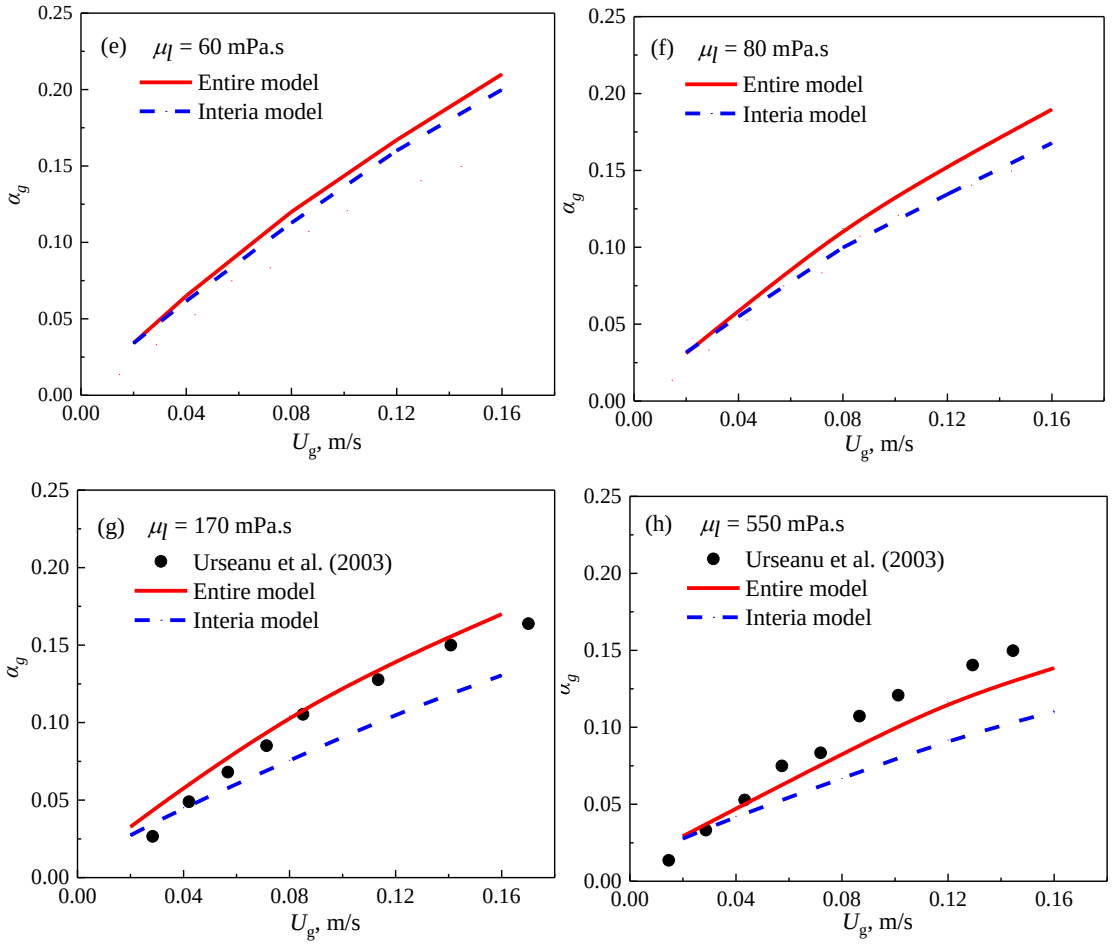

Figure 10. Comparison of the calculated average gas holdup under inertial and entire spectrum with experimental data at different liquid viscosity at ambient pressure.

6. Conclusions

The entire turbulent spectrum including the energy-containing, inertial, and energy-dissipation subranges was used to extend our previous bubble breakup model considering turbulent eddy collision based on Kolmogorov inertial subrange turbulent spectrum. The CFD-PBM coupled model with the extended bubble breakup model and previous model were used to simulate a bubble column under different pressures and liquid viscosities. The following conclusions were obtained from the simulation results and the validation with experimental data:

(1) At low liquid viscosity, the influence of gas density or pressure on the bubble breakup rate and the CFD-PBM simulations of a bubble column was little affected by the selection of turbulent spectrum.

(2) With increasing liquid viscosity, the inertial turbulent subrange narrowed and even disappeared. At high μ_l, the bubble breakup rate predicted with the inertial turbulent spectrum was greatly lower than that by the entire spectrum, and the gas holdup of a bubble column predicted by the CFD-PBM coupled model with the inertial spectrum was greatly lower than that with the entire spectrum.

(3) The CFD-PBM coupled model with the entire spectrum gave better predictions of the gas holdup of a bubble column. Therefore, in the high liquid viscosity regime, the entire spectrum should be used to include the energy-containing and energy-dissipation subranges for constructing the bubble breakup model.

(4) From the validations with the bubble breakup rate and gas holdup, the critical liquid viscosity was determined as ~80 mPa·s, above which the inertial turbulent spectrum will cause large errors and the entire spectrum should be used.

Acknowledgement

The authors thank the financial supports by the National Key Research and Development Program of China (No. 2018YFB0604804).

Notations

$b(d_b)$, $b(v)$ bubble breakup rate, s^{-1}

$c(v,v')$ bubble coalescence rate, s^{-1}

c_f factor of increase of surface energy, dimensionless

c_d	factor of increase of surface energy per unit volume, dimensionless
C, C_1	model constant, dimensionless
C_L, C_η, C_0	positive model parameters, dimensionles
C_{Di}	single bubble drag coefficient, dimensionless
C_D/C_{D0}	drag correction factor of bubble swarms, dimensionless
C_L	lift force coefficient, dimensionless
C_{TD}	turbulent dispersion force coefficient, dimensionless
C_{VM}	virtual mass force coefficient, dimensionless
C_W	wall lubrication force coefficient, dimensionless
d_{neck}	bubble neck size, m
d_b	mother bubble diameter, m
d_{c0}	critical bubble neck diameter, m
d_c	critical bubble size for differentiating small and large bubbles, m
$d_{s,j}$	local bubble Sauter diameter, m
d_{bH}	maximum horizontal dimension of the bubble, m
Eo	Eötvös number, $g(\rho_l-\rho_g)d_b^2/\sigma$, dimensionless
Eo'	corrected Eötvös number, $g(\rho_l-\rho_g)d_{bH}^2/\sigma$, dimensionless
$E(\kappa)$, $E(\lambda)$	turbulent energy spetrum, $m^3 \cdot s^{-2}$
Eo	Eötvös number, $g(\rho_l-\rho_g)d_b^2/\sigma$, dimensionless
f_i	volume fraction of bubble group i in the gas holdup, dimensionless
$f_L(\kappa L)$	non-dimensional cut-off function for energy containing subrange, dimensionless
$f_\eta(\kappa\eta)$	non-dimensional cut-off function for energy dissipation subrange, dimensionless
F	hypergeometric function required in Eqs. (13) and (16) dimensionless
F_D	drag force, $N \cdot m^{-3}$
F_L	transverse lift force, $N \cdot m^{-3}$
F_{TD}	turbulent dispersion force, $N \cdot m^{-3}$

F_{VM}	virtual mass force, $N \cdot m^{-3}$
F_W	wall lubrication force, $N \cdot m^{-3}$
k_l	gas–liquid mass transfer coefficient, ms^{-1}; kinetic energy of the liquid phase, $m^2 \cdot s^{-2}$
$k_l a$	volumetric mass transfer coefficient, s^{-1}
$k_{b,large}$	model factor for wake accelerating effect of large bubbles, dimensionless
$k_{b,small}$	model factor for hindering effect of small bubbles, dimensionless
k	turbulent kinetic energy, $m^2 \cdot s^{-2}$
K	Bessel function required in Eq. (17), dimensionless
L	integral length scale, m
n	number density of bubbles, m^{-4}
n_λ	number density of eddies, m^{-4}
$P_b(f_v' \mid d_b, \lambda)$	breakup probability, dimensionless
$P_b(f_v \mid d_b, f_v')$	breakup probability considering internal flow, dimensionless
P	pressure, MPa
P_0	model constant, dimensionless
Re_λ	Tylor-scale Reynolds number, dimensionless
Re_L	Reynolds number, $Re_L = \frac{k^{1/2} L}{\nu}$,dimensionless
S, $T_1 ... T_5$	functions for analytical solution of Eq. (11), dimensionless
t_1	internal flow time, s
t_2	neck contraction time, s
U_{neck}	internal gas flow velocity, $m \cdot s^{-1}$
U_{plus}	additional shrinking velocity, $m \cdot s^{-1}$
U_g	superficial gas velocity, $m \cdot s^{-1}$
$\bar{u}_\lambda$	the mean turbulent velocity, $m \cdot s^{-1}$
$\bar{u}$	the mean turbulent velocity at a distance of d_b, $m \cdot s^{-1}$
u_{slip}	bubble slip velocity, $m \cdot s^{-1}$

V_1	volume of smaller part of the deformed bubble, m^3

Greek letters

α_g	gas holdup, dimensionless
κ	wave number, m^{-1}
τ_e	the life span of a turbulent eddy, s
ε	turbulent energy dissipation rate, $m^2 \cdot s^{-3}$
ε_s	Volume fraction of particles, dimensionless
ρ_g	gas density, $kg \cdot m^{-3}$
ρ_l	liquid density, $kg \cdot m^{-3}$
σ	surface tension, $N \cdot m^{-1}$
λ	eddy size, m
η	Kolmogorov scale, $\eta = (\mu_l/\rho_l)^{3/4}/\varepsilon^{1/4}$, m
λ_{min}	minimum eddy size effective for breakup, m
λ_{max}	maxmum eddy size effective for breakup, m
μ_l	liquid viscosity, mPa·s
μ_{al}	apparent liquid viscosity, mPa·s
μ_g	gas viscosity, mPa·s
λ_d	defined in Eq. (19) as = $(15C)^{3/4}\eta$, m
ν	kinematic viscosity, $m^2 \cdot s^{-1}$
$\langle[\delta v]^2\rangle(\lambda)$	second-order longitudinal structure function, dimensionless
$\beta(f_v, d_b)$	daughter size distribution, dimensionless
β	model constant, dimensionless
γ	breakup probability function, dimensionless
Γ	Gamma function, dimensionless
$\varpi_\lambda(d_b)$	collision frequency density, $m^{-5} \cdot s^{-1}$
Ω	total breakup rate, $m^{-3} \cdot s^{-1}$
$\delta_{j,k}$	Dirac delta function, dimensionless
$\eta_{i,k}$	transport coefficient resulted form bubble breakup, dimensionless

$\eta_{i,jk}$ transport coefficient resulted form bubble coalescence, dimensionless

References

1. Shu SL, Vidal D, Bertrand F, Chaouki J. Multiscale multiphase phenomena in bubble column reactors: A review. *Renew Energ*. 2019;141:613-631.

2. Krishna R, Sie ST. Design and scale-up of the Fischer–Tropsch bubble column slurry reactor. *Fuel Process. Technol*. 2000;64(1):73-105.

3. Krishna R. A scale-up strategy for a commercial scale bubble column slurry reactor for Fischer-Tropsch synthesis. *Oil Gas Sci. Technol*. 2000;55(4):359-393.

4. Orvalho S, Hashida M, Zednikova M, Stanovsky P, Ruzicka MC, Sasaki S, Tomiyama A. Flow regimes in slurry bubble column: Effect of column height and particle concentration. *Chem. Eng. J*. 2018;351:799-815.

5. Urseanu MI, Guit RPM, Stankiewicz A, van Kranenburg G, Lommen JHGM. Influence of operating pressure on the gas hold-up in bubble columns for high viscous media. *Chem. Eng. Sci*. 2003;58(3-6):697-704.

6. Esmaeili A, Farag S, Guy C, Chaouki J. Effect of elevated pressure on the hydrodynamic aspects of a pilot-scale bubble column reactor operating with non-Newtonian liquids. *Chem. Eng. J*. 2016;288:377-389.

7. Esmaeili A, Guy C, Chaouki J. The effects of liquid phase rheology on the hydrodynamics of a gas–liquid bubble column reactor. *Chem. Eng. Sci*. 2015;129:193-207.

8. Kajero OT, Abdulkadir M, Abdulkareem L, Azzopardi BJ. Experimental study of viscous effects on flow pattern and bubble behavior in small diameter bubble column. *Phys. Fluids*. 2018;30(9): 093101.

9. Xing CT, Wang TF, Wang JF. Experimental study and numerical simulation with a coupled CFD–PBM model of the effect of liquid viscosity in a bubble column. *Chem. Eng. Sci.* 2013;95:313-322.

10. Kováts P, Thévenin D, Zähringer K. Influence of viscosity and surface tension on bubble dynamics and mass transfer in a model bubble column. *Int. J. Multiphase Flow*.

2020;123.

11. Wilkinson PM, Vanschayk A, Spronken JPM, Vandierendonck LL. The influence of gas-density and liquid properties on bubble breakup. *Chem. Eng. Sci*. 1993;48(7):1213-1226.

12. Lau R, Peng W, Velazquez-Vargas LG, Yang GQ, Fan LS. Gas-liquid mass transfer in high-pressure bubble columns. *Ind. Eng. Chem. Res*. 2004;43(5):1302-1311.

13. Liu L, Yan HJ, Ziegenhein T, Hessenkemper H, Li Q, Lucas D. A systematic experimental study and dimensionless analysis of bubble plume oscillations in rectangular bubble columns. *Chem. Eng. J*. 2019;372:352-362.

14. Wang TF, Wang JF, Jin Y. A CFD-PBM coupled model for gas-liquid flows. *AIChE J*. 2006;52(1):125-140.

15. Wang TF, Wang JF, Jin Y. Theoretical prediction of flow regime transition in bubble columns by the population balance model. *Chem. Eng. Sci*. 2005;60(22):6199-6209.

16. Wang TF, Wang JF. Numerical simulations of gas–liquid mass transfer in bubble columns with a CFD–PBM coupled model. *Chem. Eng. Sci*. 2007;62(24):7107-7118.

17. Yang N, Xiao Q. A mesoscale approach for population balance modeling of bubble size distribution in bubble column reactors. *Chem. Eng. Sci*. 2017;170:241-250.

18. Sarhan AR, Naser J, Brooks G. CFD modeling of bubble column: Influence of physico-chemical properties of the gas/liquid phases properties on bubble formation. *Sep. Purif. Technol*. 2018;201:130-138.

19. Liang XF, Pan H, Su YH, Luo ZH. CFD-PBM approach with modified drag model for the gas-liquid flow in a bubble column. *Chem. Eng. Res. Des*. 2016;112:88-102.

20. Liu Q, Liang XF, Luo XJ, Luo ZH. A PBM-CFD model with optimized PBM-customized drag equations for chemisorption of CO_2 in a bubble column. *Int. J. Chem. React. Eng*. 2018;16(5).

21. Liu Y, Hinrichsen O. Study on CFD-PBM turbulence closures based on k-epsilon and Reynolds stress models for heterogeneous bubble column flows. *Comput. Fluids*. 2014;105:91-100.

22. Van Tran B, Nguyen DD, Ngo SI, Lim Y-II, Kim B, Lee DH, Go KS, Nho NS. Hydrodynamics and simulation of air-water homogeneous bubble column under elevated pressure. *AIChE J.* 2019.

23. Gemello L, Plais C, Augier F, Marchisio DL. Population balance modelling of bubble columns under the heterogeneous flow regime. *Chem. Eng. J*. 2019;372:590-604.

24. Shi WB, Yang XG, Sommerfeld M,Yang J, Cai XY, Li G, Zong Y. Modelling of mass transfer for gas-liquid two-phase flow in bubble column reactor with a bubble breakage model considering bubble-induced turbulence. *Chem. Eng. J*. 2019;371:470-485.

25. Zhang XB, Luo ZH. Effects of bubble coalescence and breakup models on the simulation of bubble columns. *Chem. Eng. Sci*. 2020;226.

26. Yang GY, Zhang HH, Luo JJ, Wang TF. Drag force of bubble swarms and numerical simulations of a bubble column with a CFD-PBM coupled model. *Chem. Eng. Sci*. 2018;192:714-724.

27. Guo KY, Wang TF, Liu YF, Wang JF. CFD-PBM simulations of a bubble column with different liquid properties. *Chem. Eng. J*. 2017;329:116-127.

28. Yang GY, Guo KY, Wang TF. Numerical simulation of the bubble column at elevated pressure with a CFD-PBM coupled model. *Chem. Eng. Sci*. 2017;170:251-262.

29. Zhang HH, Yang GY, Sayyar A, Wang TF. An improved bubble breakup model in turbulent flow. *Chem. Eng. J.* 2020;386:121484.

30. Zhang HH, Sayyar A, Wang YL, Wang TF. Generality of the CFD-PBM coupled model for bubble column simulation. *Chem. Eng. Sci*. 2020;219.

31. Zhang HH, Guo KY, Wang YL, Sayyar A, Wang TF. Numerical simulations of the effect of liquid viscosity on gas-liquid mass transfer of a bubble column with a CFD-PBM coupled model. *Int. J. Heat Mass Tran*. 2020;161:120229.

32. Luo HA, Svendsen HF. Theoretical model for drop and bubble breakup in turbulent

dispersions. *AIChE J*. 1996;42(5):1225-1233.

33. Razzaghi K, Shahraki F. Theoretical model for multiple breakup of fluid particles in turbulent flow field. *AIChE J*. 2016;62(12):4508-4525.

34. Wang TF, Wang JF, Jin Y. A novel theoretical breakup kernel function for bubbles/droplets in a turbulent flow. *Chem. Eng. Sci*. 2003;58(20):4629-4637.

35. Xing CT, Wang TF, Guo KY, Wang JF. A unified theoretical model for breakup of bubbles and droplets in turbulent flows. *AIChE J*. 2015;61(4):1391-1403.

36. Zhao H, Ge W. A theoretical bubble breakup model for slurry beds or three-phase fluidized beds under high pressure. *Chem. Eng. Sci*. 2007;62(1-2):109-115.

37. Das SK. A new turbulence-induced theoretical breakage kernel in the context of the population balance equation. *Chem. Eng. Sci*. 2016;152:140-150.

38. Liao Y, Lucas D. A literature review on mechanisms and models for the coalescence process of fluid particles. *Chem. Eng. Sci*. 2010;65(10):2851-2864.

39. Solsvik J, Jakobsen HA. A review of the statistical turbulence theory required extending the population balance closure models to the entire spectrum of turbulence. *AIChE J*. 2016;62(5):1795-1820.

40. Karimi M, Andersson R. An exploratory study on fluid particles breakup rate models for the entire spectrum of turbulent energy. *Chem. Eng. Sci*. 2018;192:850-863.

41. Han LC, Gong SG, Ding YW, Fu J, Gao NN, Luo HA. Consideration of low viscous droplet breakage in the framework of the wide energy spectrum and the multiple fragments. *AIChE J*. 2015;61(7):2147-2168.

42. Han LC, Gong SG, Li YQ, Gao NN, Fu J, Luo HA, Liu ZF. Influence of energy spectrum distribution on drop breakage in turbulent flows. *Chem. Eng. Sci*. 2014;117:55-70.

43. Solsvik J, Skjervold VT, Han LC, Luo HA, Jakobsen HA. A theoretical study on drop breakup modeling in turbulent flows: The inertial subrange versus the entire spectrum of isotropic turbulence. *Chem. Eng. Sci*. 2016;149:249-265.

44. Castellano S, Carrillo L, Sheibat-Othman N, Marchisio D, Buffo A, Charton S.

Using the full turbulence spectrum for describing droplet coalescence and breakage in industrial liquid-liquid systems: Experiments and modeling. *Chem. Eng. J*. 2019;374:1420-1432.

45. Niño L, Gelves R, Ali H, Solsvik J, Jakobsen H. Applicability of a modified breakage and coalescence model based on the complete turbulence spectrum concept for CFD simulation of gas-liquid mass transfer in a stirred tank reactor. *Chem. Eng. Sci*. 2020;211:115272.

46. Tennekes H, Lumley JL, Lumley JL. A first course in turbulence. Cambridge, MA: MIT press. 1972.

47. Pope SB. Turbulent flows. Cambridge, UK: Cambridge university press. 2000.

48. Solsvik J. Turbulence modeling in the wide energy spectrum: Explicit formulas for Reynolds number dependent energy spectrum parameters. *Eur. J. Mech. B/Fluids*. 2017;61:170-176.

49. Davidson PA. Turbulence. An introduction for scientists and engineers. Oxford, UK: Oxford University Press. 2004.

50. Solsvik J, Jakobsen HA. Development of fluid particle breakup and coalescence closure models for the complete energy spectrum of isotropic turbulence. *Ind. Eng. Chem. Res*. 2016;55(5):1449-1460.

51. Sawford BL, Hunt JCR. Effects of turbulence structure, molecular diffusion and source size on scalar fluctuations in homogeneous turbulence. *J. Fluid Mech*. 1986;165:373-400.

52. Andersson R, Andersson B. Modeling the breakup of fluid particles in turbulent flows. *AIChE J*. 2006;52(6):2031-2038.

53. Wilkinson PM, Vondierendonck LL. Pressure and gas-density effects on bubble break-up and gas hold-up in bubble-columns. *Chem. Eng. Sci.* 1990;45(8):2309-2315.

54. Degaleesan S, Dudukovic M, Pan Y. Experimental study of gas-induced liquid-flow structures in bubble columns. *AIChE J*. 2001;47(9):1913-1931.

55. Rudkevitch D, Macchi A. Hydrodynamics of a high pressure three-phase fluidized

bed subject to foaming. *Can. J. Chem. Eng*. 2008;86(3):293-301.